

# Enhancing diffraction-based overlay metrology capabilities in digital holographic microscopy using model-based signal separation

Tamar van Gardingen-Cromwijk<sup>a,b,\*</sup>, Simon G. J. Mathijssen,<sup>c</sup> Marc Noordam<sup>a,b</sup>,  
Stefan Witte<sup>a,b</sup>, Johannes F. de Boer,<sup>a,b</sup> and Arie den Boef<sup>c</sup>

<sup>a</sup>Advanced Research Center for Nanolithography, Amsterdam, The Netherlands

<sup>b</sup>Vrije Universiteit, Department of Physics and Astronomy, and LaserLaB, Amsterdam, The Netherlands

<sup>c</sup>ASML Netherlands B.V., Veldhoven, The Netherlands

**ABSTRACT.** **Background:** The continuous shrink of device dimensions in the semiconductor industry drives the need to improve optical microscopy techniques that are often used in overlay metrology. Achieving sub-nanometer overlay metrology precision requires near-perfect imaging conditions and an almost complete suppression of imaging artifacts.

**Aim:** Digital holographic microscopy (DHM) has been presented as a promising new overlay tool measuring the full complex-valued field, giving one computational access to the pupil plane. The unique characteristics of a holographic imaging system in combination with prior knowledge of the object under study show the capability to advance semiconductor metrology. This technique enables a further reduction in metrology target size while also offering opportunities to improve precision.

**Approach:** We present experimental results on a model-based signal separation technique using digital pupil filtering for two different metrology challenges and demonstrate strong suppression of nuisance signals without resolution loss.

**Results:** We will present two experimental examples of different types of pupil filtering in DHM allowing for larger region-of-interest selection to improve the diffraction-based overlay metrology precision and accuracy.

**Conclusion:** We experimentally demonstrate that model-based signal separation in the pupil plane can significantly enhance the overlay metrology capabilities in cases where prior knowledge of the sample is present.

© The Authors. Published by SPIE under a Creative Commons Attribution 4.0 International License. Distribution or reproduction of this work in whole or in part requires full attribution of the original publication, including its DOI. [DOI: [10.1117/1.JMM.23.4.044006](https://doi.org/10.1117/1.JMM.23.4.044006)]

**Keywords:** overlay metrology; holographic microscopy; computational imaging

Paper 24074G received Sep. 30, 2024; revised Nov. 11, 2024; accepted Nov. 12, 2024; published Nov. 28, 2024.

## 1 Introduction

Over the years, diffraction-based overlay metrology (DBO) has been widely accepted as an optical overlay (OV) metrology technique that offers robustness and sub-nanometer precision on overlay-critical layers. In DBO metrology, the lateral alignment with respect to a previous wafer layer in the multilayer stack is measured on dedicated metrology targets consisting of overlapping gratings.<sup>1-4</sup> High overlay accuracy and robustness on smaller grating marks with low diffraction efficiency require a strong suppression of undesired signals that impact the desired signal that carries the relevant overlay information. This becomes even more relevant for metrology

\*Address all correspondence to Tamar van Gardingen-Cromwijk, [t.cromwijk@arcnl.nl](mailto:t.cromwijk@arcnl.nl)

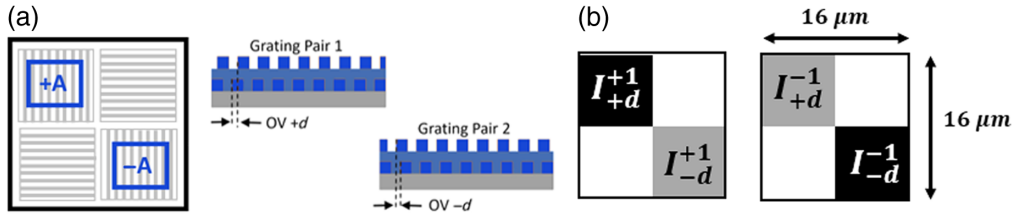


**Fig. 1** Concept of a  $\mu$ DBO target. (a) Two overlapping grating pairs with a known bias  $+d$  and  $-d$  resulting in an intensity difference  $+A$  and  $-A$ . (b) Illustrative concept of intensities on an OV target.

applications that ask for dense intrafield sampling schemes where overlay must be measured on many points in a field.<sup>5</sup> For these cases, there is a need to make the overlay target as small as possible while still maintaining good metrology precision.<sup>6,7</sup>

In DBO metrology, OV targets (e.g.,  $\mu$ DBO targets) consisting of two overlapping gratings are illuminated resulting in a  $+1^{\text{st}}$  and  $-1^{\text{st}}$  diffraction order. In the case of perfect overlap, or zero overlay, the target is symmetric, and hence, the two diffraction orders have equal intensity. Once there is a mismatch in overlap, or an “overlay error,” a difference in the intensity of the diffraction orders is measured, which scales linearly with the overlay value. As OV values are typically small compared with the pitch of the target, the intensity difference is given by

$$A = I_{+1} - I_{-1} = K \times \text{OV}, \quad (1)$$

where  $I_{+1}$  and  $I_{-1}$  are the  $+1^{\text{st}}$  and  $-1^{\text{st}}$  diffraction order intensities, respectively, and  $K$  is the unknown stack-dependent sensitivity. To determine the OV value without the knowledge of  $K$ , a known bias  $d$  is added to the OV targets, as shown in Fig. 1(a).

One grating pair has a known bias shift of  $+d$ , and the second grating pair has a known bias shift of  $-d$ . This results in four measured intensities,  $I_{+1}^{-d}$ ,  $I_{+1}^{+d}$ ,  $I_{-1}^{-d}$ , and  $I_{-1}^{+d}$ , where  $+1$  and  $-1$  refer to the diffraction orders and  $+d$  and  $-d$  to the biased pad, which is measured [Fig. 1(b)], lead to two measured intensity differences

$$A_{+} = K \times (\text{OV} + d) = I_{+1}^{+d} - I_{-1}^{+d}, \quad (2)$$

$$A_{-} = K \times (\text{OV} - d) = I_{+1}^{-d} - I_{-1}^{-d}. \quad (3)$$

Combining Eqs. (2) and (3) gives an expression for the overlay:

$$\text{OV} = d \left( \frac{A_{+} + A_{-}}{A_{+} - A_{-}} \right). \quad (4)$$

Further details on DBO and  $\mu$ DBO targets are provided in Refs. 1, 5, and 8. Currently, optical overlay metrology is measured in a dark-field microscope and requires approach subnanometer accuracy levels,<sup>4</sup> which requires intensity level measurements in DBO with a relative precision of the order of 0.01%.<sup>8</sup> Today, these precision levels are easily realized on targets with a dimension of around  $16 \times 16 \mu\text{m}^2$ . However, as mentioned earlier, dense intrafield sampling schemes ask for significantly smaller target sizes well below  $10 \times 10 \mu\text{m}^2$ .<sup>5</sup>

A reduction of the target size comes with very significant challenges and finite grating effects. For example, a smaller target suffers more from intra-target variations.<sup>5</sup> Therefore, the area where the average intensity level is calculated from, i.e., region-of-interest (RoI), should preferably cover the entire grating for small targets, as illustrated in Fig. 2(b). Moreover, a larger RoI will benefit the precision as more photons are available for the overlay measurement.

Dark-field imaging of the grating, as shown in Fig. 3(a), results in collecting the first diffraction order. For best image quality, it is desirable to completely suppress the zeroth order. In practice, however, due to the finite size of a target, a small amount of zeroth-order light leaks into the imaging optics leading to a decrease in imaging quality. This is illustrated in Fig. 3(a), where the zeroth order diffraction (indicated in red) broadens due to the finite grating size. The finite size of the grating causes a sharp change in reflectivity at the edge of the grating. The grating has a reflectivity of  $R_1$ , and the top layer has a reflectivity of  $R_0$ , as shown in Fig. 3(a).

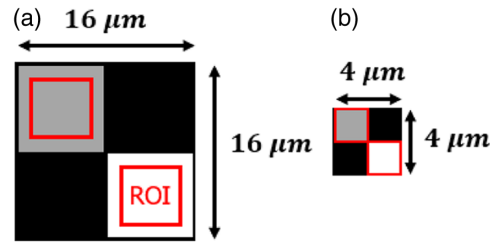


**Fig. 2** ROI selection for conventional (a) and small (b)  $\mu$ DBO targets.

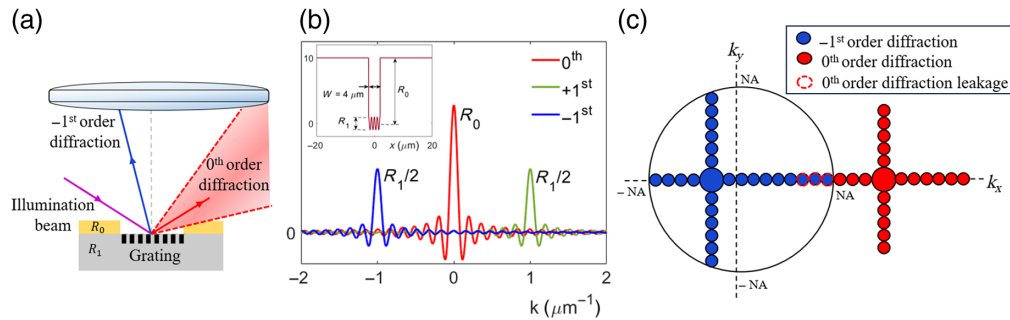


**Fig. 3** Illustration of zeroth diffraction order leakage concept in (a) dark-field configuration, (b) the 1D pupil plane, and (c) the 2D pupil plane. Purple indicates the incoming beam in panel (a), blue represents the  $-1^{\text{st}}$  diffraction order, and red represents the zeroth diffraction order.

The sharp edges of a finite grating will result in a broadening of the zeroth order signal in the spatial frequency domain. This broadening is inversely proportional to the grating size and will become quite severe for small targets that contain only a few grating lines. Figure 3(b) shows how these diffraction orders leak into each other, due to the small grating width  $W = 4 \mu\text{m}$  in combination with a reflectivity difference of the grating  $R_1$  and the top layer  $R_0$ . Figure 3(c) illustrates this broadening of the zeroth order diffraction leaking into the right side of the 2D case of a pupil, indicated by the dashed red line. In the grating image, zeroth order leakage results in a bright edge of the target and an interference pattern within the target degrading the image quality. For  $16 \times 16 \mu\text{m}^2$  size targets, the ROI can be reduced such that bright edges are excluded from the ROI, as simulated in Fig. 4(a), where the red square indicates the ROI. In the case of smaller targets (e.g.,  $4 \times 4 \mu\text{m}^2$ ), the ROI cannot be reduced because of the intratarget OV variation due to line edge roughness.<sup>5</sup> For large gratings, this effect averages out, but for small gratings, that no longer happens. The OV error due to intratarget variations can be minimized by making the ROI as large as the grating. By doing so, the bright edge ends up within the ROI, limiting the DBO metrology performance, as shown in Figs. 4(b) and 4(c).

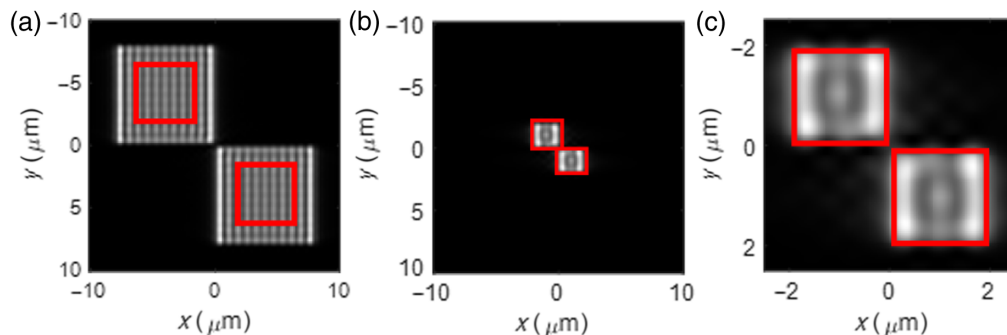


**Fig. 4** Simulation of a (a)  $16 \times 16 \mu\text{m}^2$  and (b)  $4 \times 4 \mu\text{m}^2$   $\mu$ DBO target with zeroth diffraction order leakage resulting in bright edges and (c) a magnified image of panel (b). The red box indicates the ROI.

Second, an RoI until the grating edge results in an OV measurement, which is more sensitive to light leakage from surrounding structures. Photons originating from bright surrounding structures next to the target of interest can leak into the RoI of the overlay target, influencing the accuracy of the overlay measurement. Especially, in coherent imaging systems such as digital holographic microscopy (DHM), Gibbs ringing not only leads to degradation of the image quality but also increases the optical crosstalk, i.e., light leakage from surrounding structures into the metrology target.

In this study, we will present a digital pupil filtering technique that allows us to suppress target-specific artifacts in optical overlay metrology using model-based filtering. We will demonstrate the effectiveness of our technique by presenting nuisance suppression for two different applications. This will allow for a larger RoI enabling the future use of smaller  $\mu$ DBO targets. To use digital pupil filtering techniques in dark-field microscopy, the full complex-valued field should be retrieved. This can be achieved with off-axis dark-field DHM, which has been presented as a promising new overlay metrology tool<sup>8–11</sup> and will be explained in Sec. 2.

## 2 Dark-Field Digital Holographic Microscopy

Our off-axis DHM concept distinguishes itself from other microscopy techniques by recording the image of an object as a digital hologram using a reference beam. The  $+1^{\text{st}}$  and  $-1^{\text{st}}$  diffracted beam coherently interferes with their corresponding off-axis reference fields resulting in two overlapping digital holograms on the camera sensor [Fig. 5(a)].<sup>12</sup>

The object image can be reconstructed from the digital hologram [Fig. 5(b)], using fast Fourier transform (FFT) techniques [see Figs. 5(c)–5(e)]. Using a 2D-FFT, we computationally propagate from the image plane to the pupil plane and obtain an angular spectrum with a baseband, i.e., autocorrelation signal and four sidebands [Fig. 5(c)]. The baseband is always positioned at the center of the Fourier space and does not contain any information about the phase of the object or the angle of the reference wave. The sidebands encode the amplitude and phase information of the sample image. Due to the off-axis angle configuration of the reference beams, the sidebands are fully separated from the baseband.<sup>8,13</sup> One of the sidebands is spatially filtered using a circular numerical filter, which matches with the exit pupil of the objective lens and is translated to the center of the pupil plane [Fig. 5(d)]. Finally, via an inverse Fourier transform, the object field of either the  $+1^{\text{st}}$  and  $-1^{\text{st}}$  is retrieved [Fig. 5(e)].

In the exit pupil, before an inverse Fourier transform is applied [Fig. 5(d)], a digital filter can be applied to filter the signal of interest. Such a filter can be a global window such as an apodization window,<sup>14</sup> to suppress the overall coherent ringing effects or a specific pupil window to suppress the diffracted light that should not contribute to the OV signal. The use of an

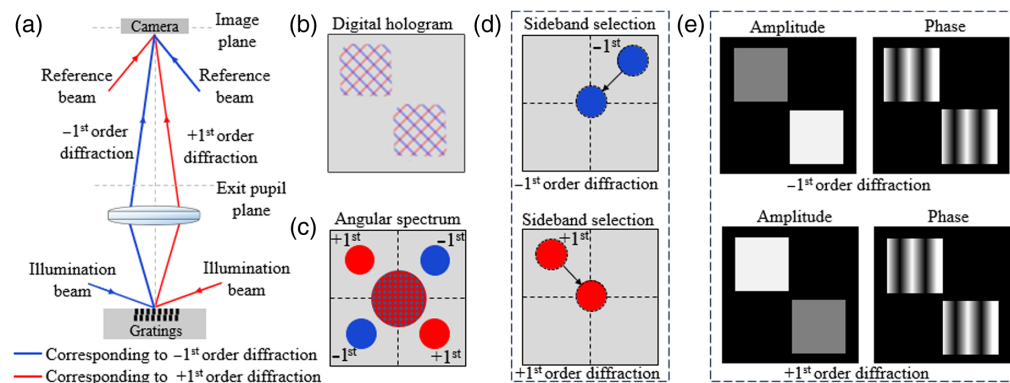


**Fig. 5** Schematic illustration of off-axis holographic recording and processing concept. (a) Schematics of the dark-field off-axis digital holography microscopy concept. (b) Recorded digital hologram with two overlapping interference patterns of the  $+1^{\text{st}}$  and  $-1^{\text{st}}$  diffraction orders. (c) The angular spectrum of the digital hologram retrieved by performing a 2D-FFT back-propagating to the pupil plane. (d) Selecting the sidebands and translating them to the center of the pupil plane. (e) Reconstructed object fields via inverse FFT of the selected sideband, resulting in the retrieval of the object amplitude and phase information.

apodization filter is a well-known solution to suppress signal imperfections. These filters do not require any prior knowledge and have been explored in our DHM concept for OV metrology as well.<sup>15</sup> Such apodization pupil filters effectively reduce Gibbs ringing effects; however, it will always be at the expense of resolution due to the broadening of the point spread function. Therefore, the main drawback of these previously studied apodizers is that images lose resolution: the target becomes more blurry. In the semiconductor industry, optical metrology is usually done on dedicated well-defined metrology targets with known dimensions. This prior knowledge of the metrology target allows the use of model-based filtering techniques that suppress undesired nuisance signals without losing spatial resolution. In Sec. 3, we will present this model-based digital pupil filter using prior knowledge of the OV metrology target and the used experimental DHM setup.

### 3 Methods

#### 3.1 Model-Based Digital Pupil Filter

In semiconductor manufacturing, the basic parameters of the overlay metrology target are typically known. Examples of such parameters are size, grating pitch, and duty cycle of the grating. Having prior knowledge of the size, geometry, or pitch of an overlay metrology target allows for designing a model-based filtering window such that only the diffracted light from the target of interest passes through the pupil. The OV metrology target, for example, consists of square gratings. Backpropagating a square grating to the pupil plane by Fourier techniques results in a 2D-sinc function,<sup>16</sup> as illustrated in Fig. 3(b). The blue 2D-sinc function illustrates the  $-1^{\text{st}}$  diffraction order in the Fourier plane, and the red 2D-sinc function indicates the zeroth diffraction order. The peak of the zeroth diffraction order is not collected in the pupil, but due to the broadening, a small portion leaks into the pupil numerical aperture (NA), indicated by the dashed red circles.

Using the prior knowledge that the zeroth diffraction order leakage shows up as a 2D-sinc function in the pupil, we can fit a model to the measured data. Such a model contains two 2D-sinc functions with a relative phase difference. After fitting the model, the zeroth diffraction order contribution can be subtracted from the measurement. This allows one to separate the first- and zeroth-order diffraction signal in the pupil and retrieve an image without the zeroth-diffraction order artifacts. The flowchart of this filter technique is presented in Fig. 6.

This model-based technique also applies to other cases where optical crosstalk can impact the quality of an overlay measurement. We can, for example, apply this method to reduce the impact of optical crosstalk from light that is diffracted by structures that surround a metrology target. This diffracted light can leak into the OV metrology target degrading the OV measurement accuracy. Reducing the impact of the signal coming from the surrounding structures could result in more robust OV metrology. To test this scenario, here, a surrounding target is filtered in the image plane, and using a Fourier transform a function, e.g., a complex 2D-sinc function, is fitted to the signal in the pupil plane. This is done for all the surrounding structures and then subtracted from the total measured signal, separating the OV signal from the surrounding signals. For both pupil filtering technique examples, an experimental result is presented and discussed in Sec. 4. Before presenting the results, we will first explain the experimental setup that we used to demonstrate our model-based filtering technique.

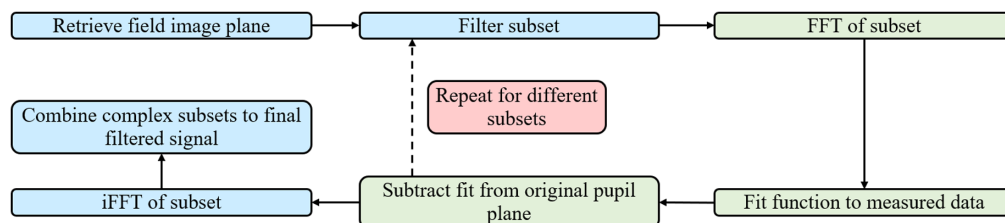


**Fig. 6** Algorithm flowchart of the pupil fitting technique, where blue and green represent the image plane and pupil plane, respectively.

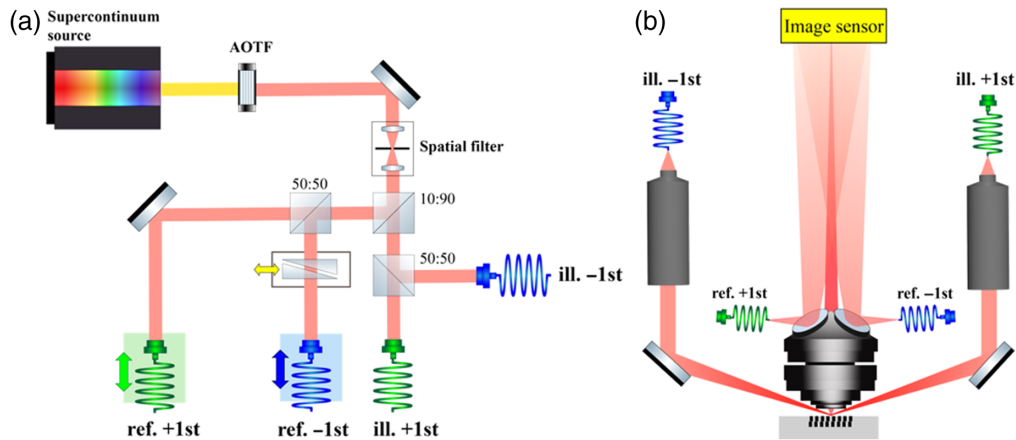


**Fig. 7** Schematic representation of the experimental setup. (a) An AOTF selects the desired wavelength coming from the spatially coherent white light source. The beam is cleaned from most of its speckles by the spatial filter, after which the beam is split in a reference and illumination beam by a 10:90 beamsplitter. 50:50 beamsplitters split the beam into two illuminations and two reference beams. The two reference beam fibers are placed on a translation stage to create two delay lines. The beams are guided via PM-PCFs to the sensor head (b). The illumination beams are diffracted on the sample via an objective under an angle of 70 deg. The imaging lens catches both the  $+1^{\text{st}}$  and  $-1^{\text{st}}$  diffraction orders. The diverging reference beams are reflected via a mirror on the camera.

### 3.2 Experimental Setup

The experimental data presented in this study were obtained using a breadboard setup of the DHM concept. A schematic representation of the setup is given in Fig. 7, similar to the setup described in Ref. 17.

The DHM-setup consists of a fiber coupled supercontinuum white light source (Leukos Rock 4005) combined with an acousto-optical tunable filter (AOTF). The AOTF provides beams with a bandwidth in the range of 3 to 8 nm and covers the visible wavelength range from 400 to 700 nm. The beam intensity from the coherent light source is split with a 90:10 beamsplitter to create an illumination and reference beam, respectively. In our DHM design, it is preferred for the object and reference beams to have nearly equal intensity. Considering the diffraction efficiency of the OV target's  $1^{\text{st}}$  diffraction order, we have selected a beamsplitter ratio of 10:90. Thereafter, a 50:50 beamsplitter is used in both paths for parallel acquisition of the  $+1^{\text{st}}$  and  $-1^{\text{st}}$  diffraction orders. The light is then coupled in polarization-maintaining photonic crystal fibers (PM-PCFs), Aeroguide-15-PM, where each reference fiber is placed on a translation stage that acts as a tunable delay line. The PM-PCFs transmit the light from the beam-splitting part [Fig. 7(a)] to the sensor head [Fig. 7(b)]. The sensor head has two off-axis illumination arms, which illuminate the target from opposite directions at an incident angle of  $\sim 70$  deg with respect to the normal plane of the sample. Light diffracted from the sample is then captured by the lens and imaged on the camera sensor. The imaging lens is a custom-made objective manufactured by Anteryon.<sup>11</sup> The objective has a numerical aperture of 0.8 and consists of two lens elements, where one lens is an asphere. The design wavelength is 650 nm. At the camera level, the  $+1^{\text{st}}$  and  $-1^{\text{st}}$  diffracted orders coming from the overlay target then coherently interfere with their corresponding reference beams resulting in two overlapping off-axis digital holograms. The image sensor is a 12-bit complementary metal-oxide semiconductor camera (Basler acA4112-8gm) with a 12 Mpixel sensor and a pixel size of  $3.45 \mu\text{m}$ . A photograph of the experimental setup is presented in Fig. 8.

### 3.3 Overlay Sample

The used overlay sample in this study consists of three layers: a bottom layer, a spacing layer, and a top layer. The bottom grating is etched in silicon with an etch depth of 100 nm. The spacing layer on top of the etched bottom grating is a 100-nm bottom anti-reflection coating. The last

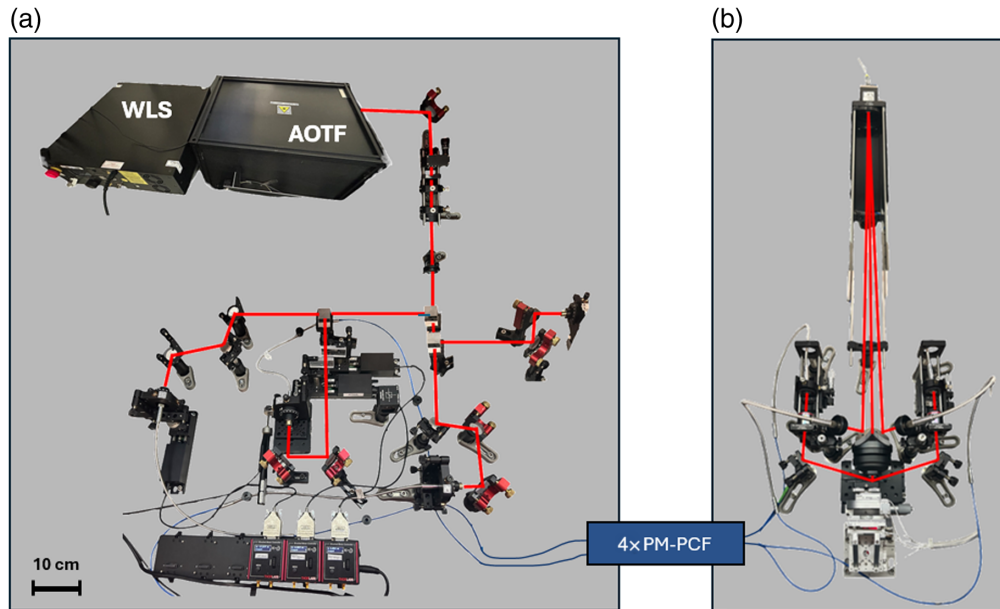


**Fig. 8** Photograph of the experimental setup, where panel (a) is the beamsplitter module and panel (b) is the sensor part.

layer in this stack, forming the top grating, is a 100-nm photo-resist layer. The used bias of the overlapping top and bottom grating is 20 nm.

## 4 Results

In DBO metrology, it is important to measure the relative intensity differences between the  $+1^{\text{st}}$  and  $-1^{\text{st}}$  diffraction order signals as accurately as possible. Any imaging artifacts or target-specific artifacts should be eliminated before extracting an overlay value. Here, we will present two experimental examples of signal separation using digital pupil filtering in DHM with the proposed fitting method from Sec. 3.1.

### 4.1 Zeroth Order Suppression

#### 4.1.1 Metrology limitation

The finite size of the grating leads to a broadening of the zeroth order signal in the spatial frequency domain. Figure 9(a) (simulation) shows this broadening of the zeroth order diffraction leaking into the right side of the pupil. In the grating image in Fig. 9(b) (simulation), this results in a bright edge of the target and an interference pattern within the target degrading the image quality and limiting the RoI size.

With digital access to the pupil plane in DHM and prior knowledge of the target geometry, we can suppress the zeroth order at the edge of the pupil. By doing so, we eliminate the increased intensity at the edges of the target and the interference pattern within the target, which allows us to select a larger RoI that helps to improve the OV metrology precision. This suppression will be done by fitting the zeroth order shape, sinc function, in the retrieved pupil of DHM and then subtracting that zeroth-order field from the pupil plane, as shown in Fig. 9(c). Here, the red line represents a sinc function fitted to the pupil plane. The subtraction of the fitted zeroth order results in a corrected pupil image [Fig. 9(d)] and its corresponding grating in the image plane, as shown in Fig. 9(e). The cross-section of the grating images [Fig. 9(f)] shows that after correction (red line), the zeroth order artifacts are decreased significantly. The bright edges are suppressed as well as the ringing behavior across the target.

Figure 10 shows a comparison between simulations of an unfiltered image (a), a filtered image using window fitting (b), and a conventional apodization window (c) (Hamming window). It is clearly visible that the bright edges of the grating are most effectively suppressed using a fitting window. Moreover, using a strong apodization window to suppress the zeroth order leakage will always be at the expense of resolution due to the broadening of the point spread function.

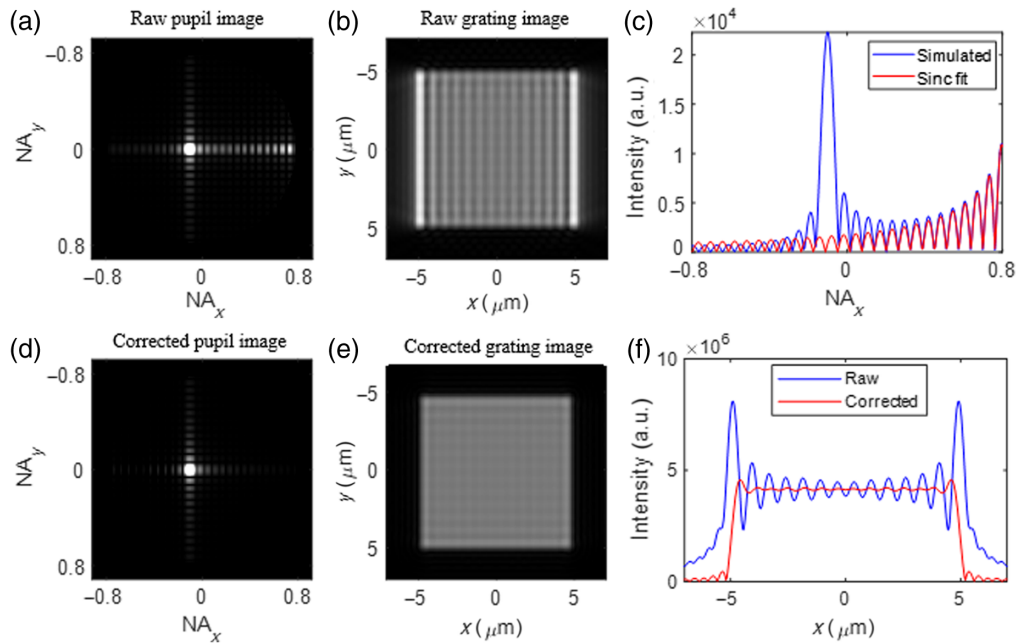


**Fig. 9** Due to the finite grating size, the zeroth order diffraction broadens and ends up leaking in the edge of the pupil (a) (simulation). This results in a bright edge in the grating image (b) (simulation). Subtraction of the fitted sinc function to the measured pupil (c) red and blue, respectively, results in a corrected pupil (d) (simulation) and the corresponding corrected grating image (e). Cross sections of grating images (f).

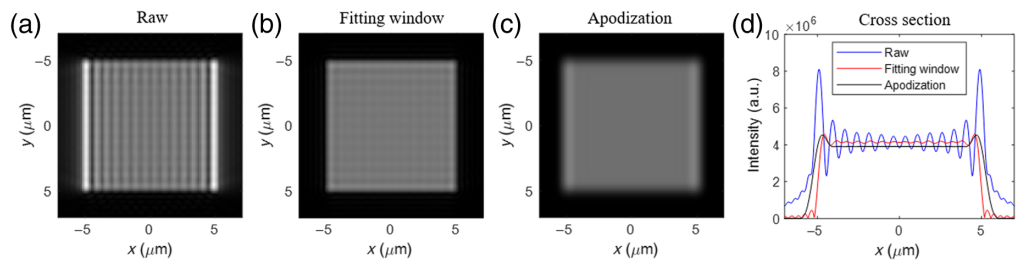


**Fig. 10** Simulated comparison of a  $10 \times 10 \mu\text{m}^2$  grating with a 600-nm pitch and measurement wavelength 632 nm, using a raw, a fitting correction, and an apodization window.

#### 4.1.2 Experimental result

We experimentally validated the approach as presented in Sec. 3.1. Figure 11 shows the experimental results of zeroth diffraction order separation and subtraction in the pupil plane.

The Fourier transform of the  $16 \times 16 \mu\text{m}^2$  OV target, [Fig. 11(a)], results in two interfering sinc functions in the pupil plane amplitude. To simplify the fitting a subset of metrology target is selected in the image plane. The Fourier transform of the subset is now a simple single sinc function, as shown in Fig. 11(b). Here, the zeroth order leakage is visible in the left edge of the pupil plane, and in the corresponding image plane [Fig. 11(c)], the zeroth order leakage is visible as clear bright lines at the edge of the grating. Moreover, an interference pattern with horizontal lines is visible in the image plane as a result of the interference between the zeroth and the first diffraction order. Fitting a sinc function to the zeroth order tail results in a function that separates the zeroth order from the other signal. By subtracting the fitted zeroth order from the measured pupil plane, we obtain a filtered pupil, as depicted in Fig. 11(d), and the corresponding image plane in Fig. 11(e). It is visible that after the zeroth diffraction order leakage is filtered out of the pupil plane, the bright edge as well as the interference pattern on the target pad are gone. Only the coherent Gibbs ringing is left, which is then suppressed using a soft apodization

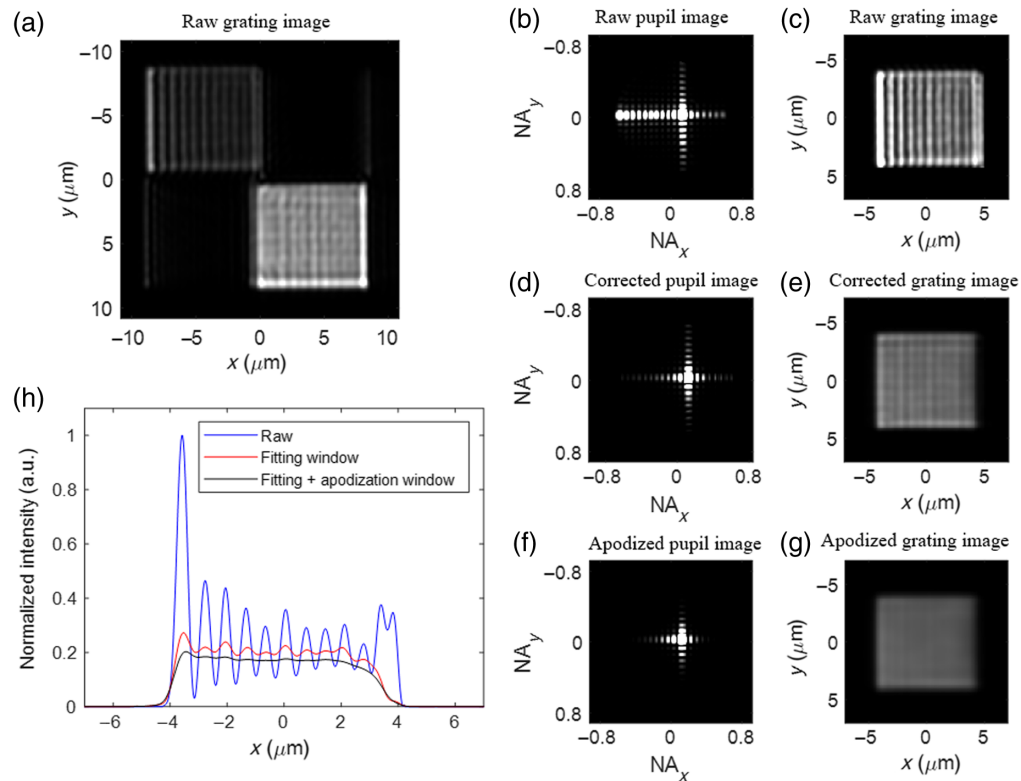


**Fig. 11** (a) A measured  $16 \times 16 \mu\text{m}^2$  overlay target with a pitch of 600 nm measured at 632 nm wavelength. (b) The Fourier transform of a subset from (a) representing the exit pupil plane in. (c) A raw grating image of the inverse FFT (b). (d) A corrected pupil image using window fitting and its corresponding corrected image (e). (f) A hamming apodized window applied to the corrected pupil plane and its corresponding grating image (g). (h) A horizontal cross-section of the grating image (c), (e), and (g).

window. Applying a soft apodization window (i.e., Hamming window) to the corrected pupil plane [Fig. 11(d)] results in Figs. 11(f) and 11(g). This analysis can be repeated for the second subset of the metrology target. The cross sections of the raw, fitted window, and fitted window with apodization window images are presented in Fig. 11(h).

With the zeroth diffraction order suppression, the target has a more homogeneous intensity distribution over the target and the bright edges, as shown in Fig. 11(h). This allows for a larger region-of-interest (RoI) selection inside the target and makes the RoI position less critical. An example of RoI selection is indicated with a red square in Fig. 12(a). The OV error as a function of a square RoI size is presented in Fig. 12.

Figure 12(g) shows the calculated OV error, using Eq. (4) with  $d = 20$  nm, as a function of RoI size for the raw intensity images (blue), zeroth diffraction order corrected (red), and zeroth diffraction order corrected with an additional soft apodization window (black). The programmed OV error of this test target equals 0 nm. The measured OV error for the raw intensity varies by 0.6 nm for a RoI size ranging from 4 to  $7 \mu\text{m}$  due to the zeroth and first diffraction order interference. When the RoI becomes larger than  $7.3 \mu\text{m}$ , the OV error increases up to 2.2 nm due to the bright target edge. With the zeroth diffraction order filtered using a fitting window in the pupil plane, the bright edge and interference pattern are removed from the signal resulting in a more homogeneous intensity, resulting in a more stable measured OV error as a function of RoI size, as shown with the red curve. The residual low frequent oscillation is caused by Gibbs ringing due to the hard cut-off of the pupil edge. This can be suppressed by applying a soft apodization window, i.e., Hamming window. After filtering the pupil and applying an apodization window, the measured OV error as a function of RoI is stable within a range of 0.2 nm. This method allows for the use of a larger RoI inside the target, resulting in more measured photons making the measurement more precise. Second, filtering out the bright edge makes the RoI position less critical.

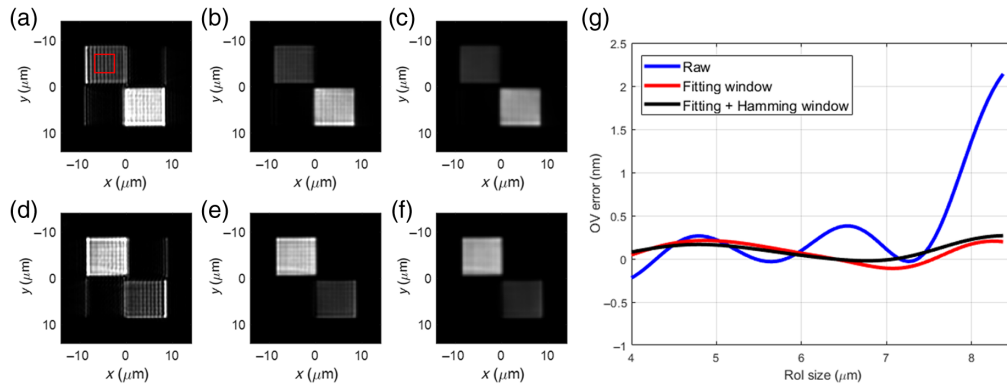


**Fig. 12** +1<sup>st</sup> (a), (b), (c) and -1<sup>st</sup> (d), (e), (f) diffraction order of a  $16 \times 16 \mu\text{m}^2$  overlay target with a pitch of 600 nm measured at 632 nm wavelength. Panels (a) and (d) show the raw intensity images, where the red box indicates an example of a RoI selection. Panels (b) and (e) have the zeroth diffraction order leakage filtered in the pupil plane using a fitting window. Panels (c) and (f) have the zeroth diffraction order leakage filtered with an additional Hamming apodization window. Panel (g) shows the calculated OV error as a function of RoI size for the three different cases.

The  $3\sigma$  static repro number is 0.5 nm for this setup. No dynamic repro numbers are available for this experimental setup.

A comparison between zeroth diffraction order filtering in combination with apodization and conventional apodization only is presented in Figs. 13(a) and 13(b), which show the measured +1<sup>st</sup> diffraction order of the OV target with a fitting window combined with apodization and apodization only, respectively. Figures 13(c) and 13(d) show this for the -1<sup>st</sup> diffraction order. The OV error as a function of square RoI size is presented in Fig. 13(e). It shows that a conventional apodization window still suffers from zeroth diffraction order leakage, degrading the OV measurement precision, whereas filtering the zeroth diffraction order using a fitting window allows for a larger RoI, which becomes especially relevant for smaller (in-die) overlay targets.

Previous presented experimental results were obtained using on  $16 \times 16 \mu\text{m}^2$  overlay targets. To verify that our zeroth order filtering method improves DBO metrology on small targets,  $4 \times 4 \mu\text{m}^2$  overlay targets with two  $2 \times 2 \mu\text{m}^2$  grating pairs were measured. The pitch of the grating is 500 nm and measured with a wavelength of 532 nm. The retrieved OV values as a function of the programmed OV are plotted in Fig. 14. The blue dots represent the measurement

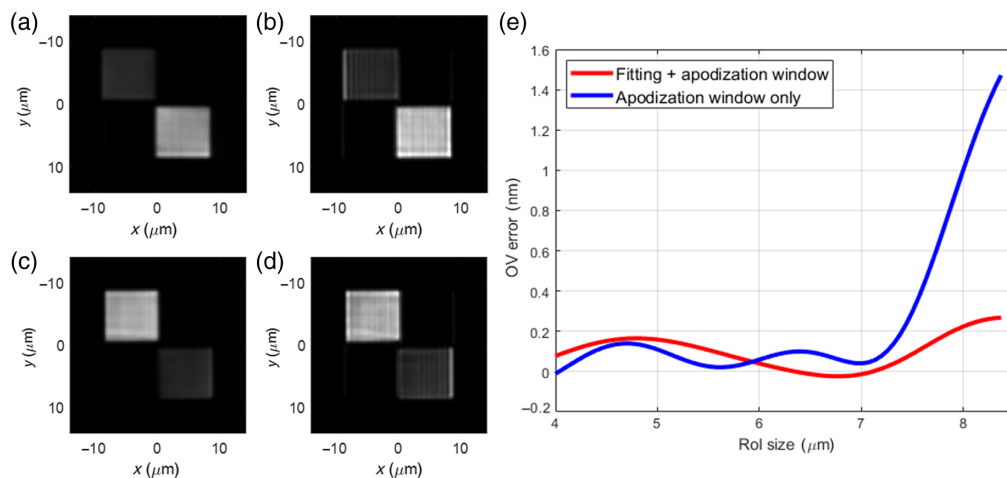


**Fig. 13** +1<sup>st</sup>, (a), (b) and -1<sup>st</sup> (c), (d) diffraction order of a  $16 \times 16 \mu\text{m}^2$  overlay target with a pitch of 600 nm measured at 632-nm wavelength. Panels (a) and (b) show the measured +1<sup>st</sup> diffraction order of the OV target with a fitting window combined with apodization and apodization only, respectively. Panels (c) and (d) show this for the -1<sup>st</sup> diffraction order. (e) OV error as a function of square RoI size, where red represents the fitting and Hamming apodization window combined and blue represents a Hamming apodization window only.

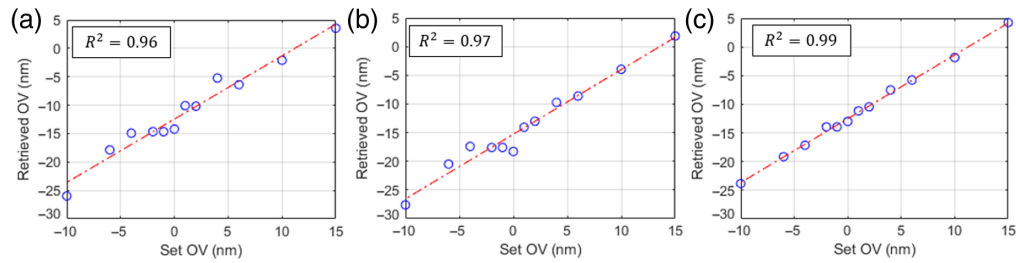


**Fig. 14** Retrieved OV values measured on  $4 \times 4 \mu\text{m}^2$  overlay targets with a pitch of 500 nm and a measurement wavelength of 532 nm. (a) Without zeroth diffraction order filtering and a RoI smaller than the grating size ( $1 \times 1 \mu\text{m}^2$ ). (b) With zeroth diffraction order filtering and a RoI smaller than the grating size ( $1 \times 1 \mu\text{m}^2$ ). (c) With zeroth diffraction order filtering and a RoI equal to the grating size ( $2 \times 2 \mu\text{m}^2$ ).

points, and the red line shows the linear fit through the retrieved OV values. Figure 14(a) represents the retrieved OV where no zeroth order suppression was applied. Therefore, the RoI was chosen to be  $1 \times 1 \mu\text{m}^2$ , which is smaller than the target size. This results in slope of 1 with an offset of  $-11.8 \text{ nm}$ . During this measurement, no Tool Induced Shift correction was applied, resulting in a constant slope offset. The relevant parameter here is  $R^2$ , which is equal to 0.96. In Fig. 14(b), the retrieved OV plot is shown with zeroth order suppression applied and a RoI equal to  $1 \times 1 \mu\text{m}^2$ . The  $R^2$  value slightly improved and is equal to 0.97. However, as presented in Fig. 12, filtering the zeroth diffraction order using a fitting window allows for a larger RoI selection. Therefore, in Fig. 14(c), we show the retrieved OV with the zeroth order filtered from the measurement and a RoI equal to the  $2 \times 2 \mu\text{m}^2$  grating size. In this case, the  $R^2$  value improves to 0.99, which is an indication of a more precise overlay measurement.

In conclusion, we have shown that model-based digital pupil filtering allows for nuisance signal reduction resulting in a larger RoI that helps to improve the precision of overlay metrology on smaller targets.

## 4.2 Model-Based Suppression of the Impact of Surrounding Structures

### 4.2.1 Metrology limitation

In addition to filtering nuisance signals from the target itself as presented in Sec. 4.1, we can also filter nuisance signals coming from structures that surround the target. Photons originating from bright surrounding structures next to the overlay metrology target can leak into the RoI, influencing the accuracy of the overlay measurement. Especially, when the RoI is equal to the grating size. Moreover, in coherent imaging systems such as DHM, Gibbs ringing not only leads to degradation of the image quality but also increases the optical crosstalk, i.e., light leakage from surrounding structures into the metrology target. As explained in Sec. 2, an apodization window can suppress coherent ringing effects. However, when the surrounding has a different grating pitch than the overlay mark, it will be asymmetrically suppressed due to the position in the pupil and the rotational symmetric origin of the apodization filter, resulting in undesired imaging artifacts. Here, we will present the first proof-of-concept experimental data that show that we can also suppress the impact of surrounding structures using a model-based filtering approach.

### 4.2.2 Experimental result

We experimentally validate the model-based digital pupil filtering for suppression surrounding structure and present the results in Fig. 15. The measured sample is a single-layer, custom-made test sample that contains two  $8 \times 8 \mu\text{m}^2$  single-layer gratings as target, having a pitch of 600 nm, and a  $16 \times 16 \mu\text{m}^2$  bright surrounding target, with a pitch of 500 nm, next to it. A hologram is measured at 632-nm wavelength.

Figure 15(a) shows the Fourier transform of the extracted image plane [Fig. 15(e)]. Due to the different pitches of the surrounding and OV structures, the diffraction orders end up at different locations in the pupil plane. The left diffraction peak [Fig. 15(a)] mainly contains the signal from the surrounding structure. Using the prior knowledge of the surrounding structure being a

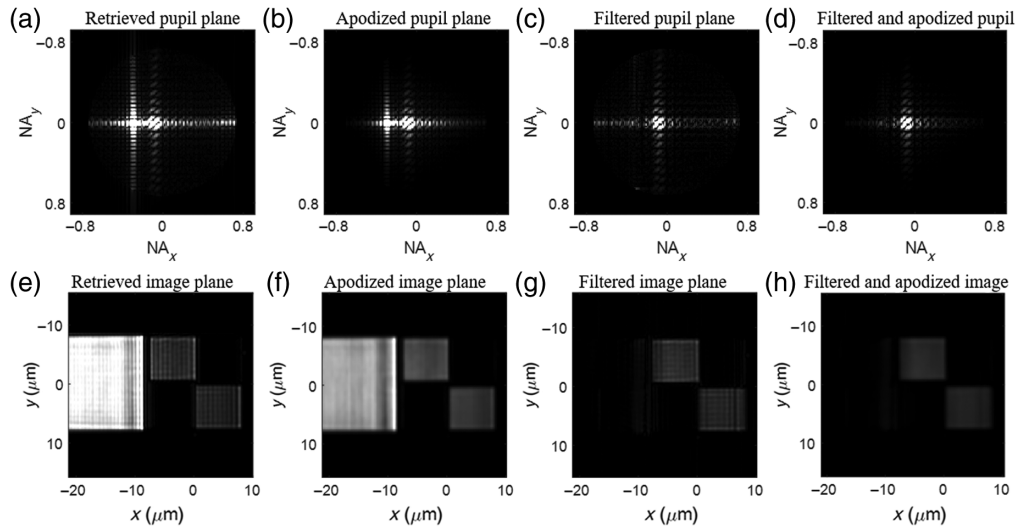


**Fig. 15** Surrounding suppression using fitting and subtraction in the pupil plane. (a) A retrieved pupil plane with a bright diffraction peak from the surrounding structure (left) and a second diffraction peak from the target (right) and its corresponding retrieved image plane (e). (b) Apodized pupil plane and its corresponding apodized image plane (f). (c) Filtered pupil plane and its corresponding filtered image plane (g). (d) Filtered pupil plane combined with a soft apodization window and its corresponding filtered image plane (h). The pitch of the surrounding target is 500 nm, and the pitch of the target is 600 nm and measured using a 632-nm wavelength.

square, one can fit a 2D-sinc function to the diffraction peak in the Fourier plane. Subtraction of the fit from the pupil plane results in a filtered pupil plane, as shown in Fig. 15(c) and its corresponding filtered image plane in Fig. 15(g). Applying a soft Hamming window to the filtered pupil, as shown in Fig. 15(d), results in a filtered image without coherent ringing [Fig. 15(h)].

This example shows that the unknown diffraction efficiency of the surrounding target can be compensated by fitting the amplitude in the pupil plane making use of the prior knowledge of the structure geometry. Therefore, the signal of the OV target can be completely separated from the surrounding signals. A conventional apodization window only as presented in Fig. 15(b) and the corresponding image plane in Fig. 15(f) reduces the sidelobes and therefore the light leakage into the OV target. However, apodization loses resolution, and therefore, the edges of the surrounding structure broaden as well and leak into the target structure. With the computational surrounding fitting method, the field from the surrounding structure is completely filtered without the loss of resolution. Therefore, the optical crosstalk between neighboring structures is suppressed, which helps to improve metrology precision.

## 5 Conclusion

In conclusion, we demonstrated that in our DHM concept, where we retrieve the full complex field, we are able to separate signals of interest through model-based digital filtering in the pupil plane. We presented two experimental examples of different types of pupil filtering in DHM allowing for larger RoI selection to improve the DBO metrology precision and accuracy.

First, we demonstrated the zeroth order (i.e., specular reflection) suppression resulting in a reduction of the bright edges of an overlay target and the interference pattern inside the OV target. This allows one to use a larger RoI inside the target and makes the RoI position less critical. Second, we presented a pupil filtering technique to separate the signal of interest from additional signals coming from surrounding structures. Therefore, the optical crosstalk leaking into the OV target can be strongly suppressed.

To reach the sub-nm precision of OV metrology, we push the capabilities of computational imaging methods and DHM well beyond their existing boundaries. This study experimentally demonstrates that model-based signal separation in the pupil plane can significantly enhance the overlay metrology capabilities in cases where prior knowledge of the sample is present.

## Disclosures

The authors declare no conflicts of interest. The authors declare that they have patents or patent applications. Simon G.J. Mathijssen and Arie den Boef are employees of ASML.

## Code and Data Availability

Data underlying the results presented in this paper are not publicly available at this time but may be obtained from the authors upon reasonable request.

## Acknowledgments

This work was conducted at the Advanced Research Center for Nanolithography, a public-private partnership between the University of Amsterdam (UvA), Vrije Universiteit Amsterdam (VU), Rijksuniversiteit Groningen (RUG), the Netherlands Organization for Scientific Research (NWO), and the semiconductor equipment manufacturer ASML.

## References

1. A. J. den Boef, "Optical wafer metrology sensors for process-robust CD and overlay control in semiconductor device manufacturing," *Surf. Topogr.: Metrol. Properties* **4**(2), 023001 (2016).
2. P. Leray et al., "Diffraction based overlay metrology: accuracy and performance on front end stack," *Proc. SPIE* **6922**, 69220O (2008).
3. W. D. Yang et al., "Novel diffraction-based spectroscopic method for overlay metrology," *Proc. SPIE* **5038**, 200–207 (2003).
4. M. Adel et al., "Diffraction order control in overlay metrology: a review of the roadmap options," *Proc. SPIE* **6922**, 692202 (2008).
5. S. Mathijssen et al., "Color mixing in overlay metrology for greater accuracy and robustness," *Proc. SPIE* **10959**, 109591G (2019).
6. A. Salerno et al., "Enabling optical metrology on small  $5 \times 5 \mu\text{m}^2$  in-cell targets to support flexible sampling and higher order overlay and CD control for advanced logic devices nodes," *Proc. SPIE* **10585**, 105851I (2018).
7. N. Smith, B. Peterson, and G. Goelzer, "Size matters in overlay measurement," *Proc. SPIE* **8324**, 832418 (2012).
8. C. Messinis et al., "Diffraction-based overlay metrology using angular-multiplexed acquisition of dark-field digital holograms," *Opt. Express* **28**(25), 37419–37435 (2020).
9. M. Adhikary et al., "Illumination spot profile correction in digital holographic microscopy for overlay metrology," *J. Micro/Nanopattern. Mater. Metrol.* **22**(2), 024001 (2023).
10. T. T. van Schaijk et al., "Diffraction-based overlay metrology from visible to infrared wavelengths using a single sensor," *J. Micro/Nanopattern. Mater. Metrol.* **21**(1), 014001 (2022).
11. T. van Gardingen-Cromwijk et al., "Non-isoplanatic lens aberration correction in dark-field digital holographic microscopy for semiconductor metrology," *Light: Adv. Manuf.* **4**, 453 (2023).
12. U. Schnars and W. Jüptner, "Direct recording of holograms by a CCD target and numerical reconstruction," *Appl. Opt.* **33**(2), 179–181 (1994).
13. A. Doblas et al., "Study of spatial lateral resolution in off-axis digital holographic microscopy," *Opt. Commun.* **352**, 63–69 (2015).
14. F. Harris, "On the use of windows for harmonic analysis with the discrete Fourier transform," *Proc. IEEE* **66**(1), 51–83 (1978).
15. C. Messinis et al., "Pupil apodization in digital holographic microscopy for reduction of coherent imaging effects," *Opt. Contin.* **1**, 1202–1217 (2022).
16. J. W. Goodman, "Introduction to Fourier optics," in *Introduction to Fourier Optics*, J. W. Goodman, Ed., 3rd ed., Vol. **1**, Roberts & Co. Publishers, Englewood, CO (2005).
17. T. van Gardingen-Cromwijk et al., "Field-position dependent apodization in dark-field digital holographic microscopy for semiconductor metrology," *Opt. Express* **31**(1), 411–425 (2023).

**Tamar van Gardingen-Cromwijk** is currently a PhD candidate at the Advanced Research Center for Nanolithography (ARCNL) in Amsterdam, and the Vrije Universiteit, Amsterdam. She received her BSc and MSc degrees in applied physics from Eindhoven University of Technology in 2019 and 2021, respectively. The goal of her PhD research is the development of a metrology tool based on digital holography, capable of robust semiconductor metrology with the aid of computational algorithms.

**Simon G. J. Mathijssen** received his PhD in applied physics from Eindhoven University of Technology in 2010, working in the field of organic electronics. After his PhD, he moved to ASML research where he worked on a variety of optical sensor techniques. Currently, he is an ASML fellow and head of the pathfinding group in business line applications at ASML, where he works on current and future-generation wafer metrology techniques.

**Marc Noordam** received his PhD in experimental physics from Delft University of Technology, where he focused on nanophotonics in 2D materials and plasmonic systems. Currently, he is a postdoctoral researcher at ARCNL, developing novel microscopy systems for OV metrology.

**Stefan Witte** is a professor of optics for nanoscale metrology, in the Imaging Physics Department of the Faculty of Applied Sciences. He received his PhD from the Vrije Universiteit Amsterdam in 2007. His research interests include coherent diffractive imaging with visible and EUV radiation, high-harmonic generation and its applications, photoacoustic imaging, and advanced laser development for plasma experiments.

**Johannes F. de Boer** is a full professor and department head of the Physics and Astronomy Department of the Vrije Universiteit, Amsterdam. He received his PhD in experimental optics from the University of Amsterdam in 1995. His research focuses on optical coherence tomography and light interferometry for biomedical imaging and metrology in scattering samples, and the characterization of local polarization properties.

**Arie den Boef** received his degree in electrical engineering from the Eindhoven Polytechnic Institute and his PhD from the University of Twente. He worked at Philips from 1979 to 1997 where he worked in the area of laser diodes, optics, MRI, and optical storage. He joined ASML in 1997, where he explored various optical metrology techniques. He is also a part-time full professor at the Vrije Universiteit of Amsterdam and leads the group of Computational Imaging at ARCNL.